Charge exchange, excitation, and ionization in $H(1s)+He^{2+}$ collisions simulated using the multichannel perturbed-stationary-state propagator

Gabriel Hose
The James Franck Institute, The University of Chicago, Chicago, Illinois 60637
(Received 16 September 1996; revised manuscript received 15 April 1997)

I recently reported [Phys. Rev. A **51**, 2222 (1995)] on simulations of charge-exchange and excitation processes in collisions between a helium nucleus and a ground-state hydrogen atom that were performed in the multichannel perturbed-stationary-state framework without employing electron translation factors [Phys. Rev. A **51**, 2199 (1995)]. A simulation with 45 adiabatic molecular orbitals reproduced the measured cross sections for electron capture and for the ensuing Lyman fluorescence lines of He^+, up to the collisional ionization threshold (~ 9 keV/amu). In this study, the collision of He^{2+} on $H(1s)$ is investigated further using a multichannel propagator defined over the former perturbed-stationary-state basis extended to include 35 L^2 ionization pseudostates of the linear combination of atomic orbitals (LCAO) type. The simulated total charge-transfer cross section is now in good agreement with experiment across the peak plateau and well into the falloff wing, where it begins to tail away at energies above 30 keV/amu because the LCAO ionization set is deficient. Concurrently, throughout the range where collisional ionization is important, state-selective cross sections are improved compared to our previous study. Approximately 25% of the calculated peak transfer cross section is associated with $n \geqslant 3$ He^+ levels. The multichannel propagator simulations imply that (i) decay cascades contribute almost one-third of the ensuing spontaneous He II Lyman-α fluorescence cross section [J. Phys. B **24**, 4025 (1991)] that is accurately reproduced and (ii) capture-induced Balmer-α and Paschen-α emissions are considerably stronger than the values either measured in the aforementioned experiment or computed by translation-factor models. [S1050-2947(97)04608-8]

PACS number(s): 34.10.+x, 34.50.Pi, 34.70.+e

I. INTRODUCTION

The one-electron collision system $H(1s)+He^{2+}$ has been studied extensively in experiments [1–13] and by theoretical models [14–36]. This is perhaps the simplest system exhibiting profound reactive and inelastic scattering phenomena accessible to both accurate measurements and tractable calculations. Not too long ago, we have advanced [37] a multichannel perturbed-stationary-state (PSS) framework to simulate electron capture and excitation processes in collisions involving ionic and atomic species. Our time-dependent close-coupling model is derived without resorting to electron translation factors and yet provides a complete and unique description of the collision including state-specific cross sections. An initial application of the multichannel propagator formalism [37] immediately followed [36] with simulations of $H(1s)+He^{2+}$ and $He^+(1s)+H^+$ collisions using adiabatic orbital bases of varying size. Up to the ionization threshold, the cross sections calculated for the nonresonant charge-transfer reaction $H(1s)+He^{2+}\rightarrow H^+ + He^+$ converge to the experimental values as the number of molecular orbitals is increased. For center-of-mass collision velocities below 0.7 a.u. the total and partial electron-capture cross sections calculated using the lowest 45 orbitals agree with the experiment well within the measurement error. Above the velocity of ~ 0.6 a.u. (9 keV/amu), collisional induced ionization kicks in and must be reckoned with. In this range our previous study [36], which employs only bound-electron states, failed to accurately describe the charge-exchange cross section. In this work we augmented the previous adiabatic basis set [36] with positive-energy L^2 orbitals representing ionization functions and repeated the $H(1s)+He^{2+}$ collision simulations. Section II provides a brief review of the multichannel PSS theory [37] and discusses how it is adapted to include the ionization channel. The calculation of reliable adiabatic ionization orbitals and the associated dynamical couplings within the linear combination of atomic orbitals (LCAO) framework is described in Sec. III. Simulation results are presented and discussed in Sec. IV, and Sec. V is summary. Atomic units ($\hbar=1$, $m_e=1$, $e=1$) are used everywhere below.

II. THEORY

Consider a system comprising an α particle, a proton, and one electron, whose instantaneous configuration is given by the laboratory-frame position vectors $\vec{X}_{\mathrm{He}}$, $\vec{X}_{\mathrm{H}}$, and $\vec{X}_e$, respectively. A body-fixed internal coordinate frame is defined using the internuclear ($\vec{R}$) and electron ($\vec{r}$) vectors [36–38]

$$\vec{R}=\vec{X}_{\mathrm{H}}-\vec{X}_{\mathrm{He}}, \quad \vec{r}=\vec{X}_e-p\vec{X}_{\mathrm{He}}-q\vec{X}_{\mathrm{H}}, \quad p+q=1, \quad (1)$$

and taking the electronic $\hat{z}$ axis to coincide with $\vec{R}$ [39,40]. The transformation (1) places the electron origin somewhere on the line joining the nuclei. Though all the calculations below are performed for one particular choice of p and q, the same results are obtained with any other origin. This is because the dynamical operators involved in the collision simulations are strictly Galilean invariant and would remain so when properly transformed [37,41] to *any arbitrary internal frame*. Notice that in the coordinates (1) the internal ki-

netic energy is not diagonal, unless p and q correspond to the nuclear center of mass [37,39,41].

A. Electronic basis states

In the perturbed-stationary-state approach [14,15,36–39,42–45], the wave function of the electron Ψ is expanded in the adiabatic Born-Oppenheimer (BO) electronic states $\{\psi_\alpha\}$ satisfying

$$H_{\rm BO}(R;\vec{r})\,\psi_\alpha(\vec{R};\vec{r}) = U_\alpha(R)\,\psi_\alpha(\vec{R};\vec{r}), \tag{2}$$

where $H_{\rm BO}$ is the electronic Hamiltonian

$$H_{\rm BO}(R;\vec{r}) = -\frac{1}{2}\,\Delta_r - \frac{2}{|\vec{r}+q\vec{R}|} - \frac{1}{|\vec{r}-p\vec{R}|}. \tag{3}$$

Given the value of R, the solution of the eigenvalue equation (2) is independent of the particular choice of p and q since it provides the states of an electron in a fixed cylindrical field of He^{2+} and H^+.

The adiabatic electronic energies $\{U_\alpha\}$ are continuous implicit functions of R, while the molecular orbitals $\{\psi_\alpha\}$ exhibit an implicit dependence on the entire vector $\vec{R}$, which defines the laboratory orientation of the electronic body-fixed frame. As the adiabatic orbitals and energies both continuously vary with R, the following direct-sum decompositions are self-evident on considering the limit $R\to\infty$ [36,37,46–51]:

$$\{\psi_\alpha\} = \{\psi_\alpha^{\rm He}\}\oplus\{\psi_\alpha^{\rm H}\}\oplus\{\psi_\alpha^{\rm I}\}, \quad \{U_\alpha\} = \{U_\alpha^{\rm He}\}\oplus\{U_\alpha^{\rm H}\}\oplus\{U_\alpha^{\rm I}\}. \tag{4}$$

The orthogonal subspaces $\{\psi_\alpha^{\rm He}\}$ and $\{\psi_\alpha^{\rm H}\}$ contain molecular orbitals whose $R\to 0$ limits are the bound Li^{2+} states [36,46–48]. Due to this isomorphism the molecular orbitals are usually labeled by the united-atom principal (energy), angular, and magnetic quantum numbers n, l, and m [46]. The third subset $\{\psi_\alpha^{\rm I}\}$ consists of adiabatic ionization states and is isomorphic with the continuum eigenstates of Li^{2+} [36,49,50]. The ionization energy curves $\{U_\alpha^{\rm I}=\varepsilon\}$ are therefore constant functions of R [49,50] and ε replaces the integer principal number n in the label α for continuum orbitals. In the limit $r\to\infty$ the ionization states $\{\psi_\alpha^{\rm I}\}$ are superpositions of Li^{2+} Coulomb waves with R-dependent phase shifts [49,50]. Accordingly, they represent the ionized-electron probability amplitude relative to the molecular center of charge.

In the limit $R\to\infty$, molecular orbitals from the subsets $\{\psi_\alpha^{\rm He}\}$ and $\{\psi_\alpha^{\rm H}\}$, respectively, become the zero-field limit Stark orbitals [36,46] of the helium ion and hydrogen atom. These limiting Stark states are known [36] superpositions of degenerate atomic orbitals of the helium ion ($\{\phi_{nlm}^{\rm He^+}\}$) and hydrogen atom ($\{\phi_{nlm}^{\rm H}\}$), namely,

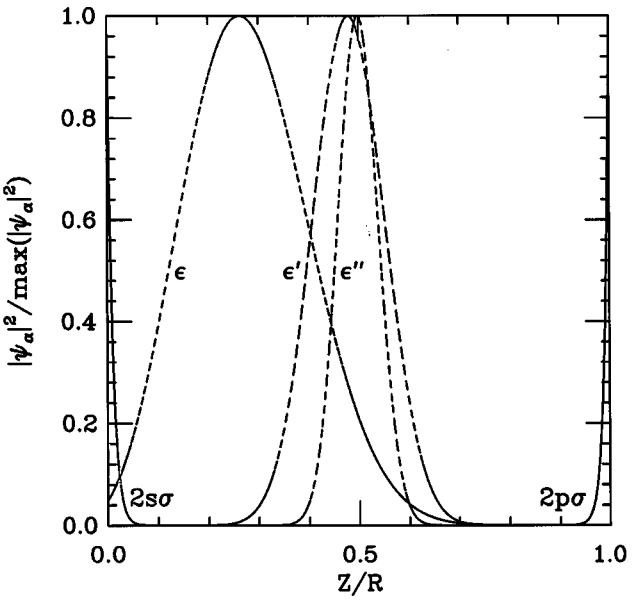

FIG. 1. Relative probability of finding the electron on the internuclear axis between He($Z=0$) and H($Z=R$) computed at $R=50$ bohrs for the two bound orbitals $2s\sigma$ and $2p\sigma$ (solid lines) and three σ adiabatic continuum functions (broken lines) of HeH^{2+} at the ionization energies $\epsilon=0.05$, $\epsilon'=0.5$, and $\epsilon''=5.0$ hartree.

$$\lim_{R\to\infty}\psi_\alpha^{\rm He}(\vec{R};\vec{r}) \to \sum_{l=|m|}^{n-1}\langle nlm|\alpha\rangle\,\phi_{nlm}^{\rm He^+}(\vec{r}+q\vec{R}), \tag{5a}$$

$$\lim_{R\to\infty}U_\alpha^{\rm He}(R)\to U_n^{\rm He^+},$$

$$\lim_{R\to\infty}\psi_\alpha^{\rm H}(\vec{R};\vec{r}) \to \sum_{l=|m|}^{n-1}\langle nlm|\alpha\rangle\,\phi_{mlm}^{\rm H}(\vec{r}-p\vec{R}), \tag{5b}$$

$$\lim_{R\to\infty}U_\alpha^{\rm H}(R)\to U_n^{\rm H}.$$

Here $U_n^{\rm He^+}$ and $U_n^{\rm H}$ are the limit ion and atom energies, n and l are the free-species principal and centrifugal quantum numbers, m is a magnetic number identical to the united-atom value of ψ_α, and $\{\langle nlm|\alpha\rangle\}$ are the Stark coefficients whose calculation was previously discussed [36].

Contrary to the bound-electron adiabatic orbitals that asymptotically become atomic functions, the $R\to\infty$ limit of the ionization states $\{\psi_\alpha^{\rm I}\}$ retains a ''molecular'' character. These are spatially extended continuum states, and as such, for all R necessarily describe the electron motion in the entire field of the nuclei He^{2+} and H^+. The large R nature of the adiabatic states is demonstrated in Fig. 1, which depicts the exact [47–50] probability of finding the electron along the internuclear axis at $R=50$ bohrs for three adiabatic continuum states and two bound molecular orbitals having different dissociation limits. It is evident from the figure that in the limit $R\to\infty$, the three subspaces $\{\psi_\alpha^{\rm He}\}$, $\{\psi_\alpha^{\rm H}\}$, and $\{\psi_\alpha^{\rm I}\}$, represent the three possible asymptotic arrangements of the electron (and the system): the helium ion, hydrogen atom, and ionized (free) electron.

B. Multichannel close-coupling equations

Since the adiabatic basis (4) is complete for all R by virtue of the Schrödinger equation (2), the temporal electron wave function can formally be expressed as a linear superposition of stationary adiabatic states with time-dependent coefficients. Including the ionization continuum explicitly the result is

$$\Psi(\vec{R};\vec{r},t)=\sum_{l,m}\int a^{\mathrm{I}}_{\epsilon lm}(t)\psi^{\mathrm{I}}_{\epsilon lm}(\vec{R};\vec{r})\rho(\epsilon)d\epsilon + \sum_{\nu=\mathrm{He,H}}\sum_{\alpha\in\nu} a^{\nu}_{\alpha}(t)\psi^{\nu}_{\alpha}(\vec{R};\vec{r}), \tag{6}$$

where $\rho(\varepsilon)$ is the continuum density at the ionization energy ε, l and m are the united-atom angular and magnetic numbers, and $\alpha=(n,l,m)\in\nu$ means the summation over $\{\psi^{\nu}_{\alpha}\}$ with n the united-atom principal number labeling bound orbitals. In the semiclassical eikonal approximation [42–45], the temporal adiabatic-state amplitudes at the scattering energy E satisfy a set of coupled differential equations along a straight-line nuclear trajectory running parallel to the nuclear $\hat{Z}$ axis at the impact parameter b (the nuclear polar radius). To solve the coupled equations corresponding to the expansion (6) it is necessary in practice to discretize the ionization continuum. A useful approach [31,32,53–60] is to represent the subset $\{\psi^{\mathrm{I}}_{\alpha}\}$ by L^2 pseudostates that properly span the quasimolecule region where the collisional ionization couplings are confined. Pseudoionization states are similar to bound orbitals but have positive energies. The multichannel PSS coupled equations therefore have the form [37]

$$i\frac{da^{\nu}_{\alpha}}{dZ}=\sum_{\lambda=\mathrm{He,H,I}}\sum_{\beta\in\lambda}\langle\psi^{\nu}_{\alpha}|G(Z,b,E)|\psi^{\lambda}_{\beta}\rangle a^{\lambda}_{\beta},\quad \nu=\mathrm{He,H,I}, \tag{7}$$

with the temporal expansion coefficients being functions of Z via $t=Z/V$, where V is the nuclear velocity, which is assumed to be constant, defining the $\hat{Z}$ direction.

The multichannel propagator G in Eq. (7) is an effective operator defined [37,52] as the temporal weighted average of the single-channel propagators associated with the possible asymptotic two-fragment arrangements of He^{2+}, H^+, and the electron. Here G is the average of two eikonal propagators G_{He} and G_{H} [37],

$$G(Z,b,E)=W_{\mathrm{He}}(Z,b,E)G_{\mathrm{He}}(Z,b,E) + W_{\mathrm{H}}(Z,b,E)G_{\mathrm{H}}(Z,b,E), \tag{8}$$

with the weights being determined from the instantaneous adiabatic-state amplitudes (see below) according to

$$W_{\nu}(Z,b,E)=\sum_{\alpha\in\nu}|a^{\nu}_{\alpha}(Z,b,E)|^2+\tfrac{1}{2}\sum_{\alpha\in\mathrm{I}}|a^{\mathrm{I}}_{\alpha}(Z,b,E)|^2,\quad \nu=\mathrm{He,H}. \tag{9}$$

The single-channel propagators G_{He} and G_{H} are generated [37] by the scattering-energy operators for the two-fragment arrangements $He^+ + H^+$ and $H + He^{2+}$, respectively. The matrix elements of G_{ν} in the adiabatic basis $\{\psi_{\alpha}\}$ are given by [37]

$$\langle\psi_{\alpha}|G_{\nu}(Z,b,E)|\psi_{\beta}\rangle=V_{\nu}^{-1}U_{\alpha}\delta_{\alpha,\beta}-iR^{-1}\langle\psi_{\alpha}|ZA^{R}_{\nu} - bA^{\theta}_{\nu}|\psi_{\beta}\rangle,\quad \nu=\mathrm{He,H}, \tag{10}$$

where $R=(Z^2+b^2)^{1/2}$ is the internuclear distance, $V_{\nu}=(2\mu_{\nu}^{-1}E)^{-1/2}$ is the collision velocity in the arrangement ν with reduced scattering mass μ_{ν} [e.g., $\mu_{\mathrm{He}}^{-1}=(m_{\mathrm{He}}+1)^{-1}+m_{\mathrm{H}}^{-1}$], and

$$A^{R}_{\nu}=\frac{\partial}{\partial R}+(p\,\delta_{\nu,\mathrm{H}}-q\,\delta_{\nu,\mathrm{He}})\frac{\partial}{\partial z},\qquad A^{\theta}_{\nu}=-iR^{-1}L_y+(p\,\delta_{\nu,\mathrm{H}}-q\,\delta_{\nu,\mathrm{He}})\frac{\partial}{\partial x}. \tag{11}$$

The electronic coupling operators A^{R}_{ν} and A^{θ}_{ν} equal $-i$ times the radial and angular components of the scattering momentum operator in the νth rearrangement channel and are therefore Galilean invariant [37,41,51]. That is, the matrix elements (10) are independent of the electronic origin parameters p and q [Eq. (1)] and the coupled equations (7) have a unique solution determined solely by the initial conditions [37].

A two-body scattering momentum must be defined within a Jacobi coordinate frame. Accordingly, the weight W_{ν} of a propagator in Eq. (8) is the instantaneous probability of occupying the Jacobi frame appropriate to define the (asymptotic) kinetic energy of the corresponding fragments [37,52]. The weight (9) is the probability of finding the system in the bound-orbital subspace $\{\psi^{\nu}_{\alpha}\}$ plus one-half of the ionization probability. Formula (9) emerges from topological considerations. Remember that while the molecular orbitals $\{\psi^{\nu}_{\alpha}\}$ vary continuously toward asymptotic linear combinations [Eqs. (5)] of bound-electron atomic (or ionic) states $\{\phi^{\nu}_{nlm}\}$, the adiabatic continuum functions $\{\psi^{\mathrm{I}}_{\alpha}\}$ in the limit $R\to\infty$ describe electron motion relative to a molecular center (Fig. 1). That is, $\{\psi^{\mathrm{I}}_{\alpha}\}$ is not an asymptotic atomic continuum subset. Rather, $\{\psi^{\mathrm{I}}_{\alpha}\}$ is contained in the atomic (or ionic) ionization subset $\{\phi^{\nu}_{\varepsilon lm}\}$ since the subspace $\{\psi^{\nu}_{\alpha}\}$ is isomorphic with $\{\phi^{\nu}_{nlmn}\}$ and $\{\phi^{\nu}_{nlmn}\}\oplus\{\phi^{\nu}_{\epsilon lm}\}$ is equivalent to the complete adiabatic basis (4). So clearly, $\{\phi^{\nu}_{\varepsilon lm}\}=\{\psi^{\lambda\neq\nu}_{\alpha}\}\oplus\{\psi^{\mathrm{I}}_{\alpha}\}$, which implies that the breakup set $\{\psi^{\mathrm{I}}_{\alpha}\}$ is shared between the asymptotic two-fragment arrangements, whence follows the one-half factor in Eq. (9) as there are only two asymptotic bound-electron arrangements: $He^+ + H^+$ and $H + He^{2+}$.

The multichannel propagator (8) is instantaneously averaged over the channel eikonal propagators according to the temporal charge-transfer and ionization probabilities. Beginning with the incoming-channel component, its composition (i.e., entire coupling profiles as a function of R) varies continuously throughout the interaction region as specified by the initial scattering conditions (state and energy). The propagator (8) hence differs manifestly from other semiclassical models that employ time-independent composite couplings, obtained, for instance, (i) by averaging over origins

weighted by the electron stationary-state probability amplitudes [61], (ii) by using many origins as defined by the coupled Gaussian basis functions [62], and (iii) from an R-matrix propagation spanning a PSS basis in the quasimolecular region and, after proper matching, an atomic basis at large R [63]. Unlike the multichannel approach, these three procedures do not permit an instantaneous temporal change in the propagator composition and are characterized by spatial coupling profiles that remain constant in time.

C. Asymptotic analysis

In this study the process of electron capture in the collision of He^{2+} on $H(1s)$ is simulated with exact molecular orbitals from $\{\psi_\alpha^{He}\}$ and $\{\psi_\alpha^{H}\}$ [36] and an ionization set $\{\psi_\alpha^{I}\}$ modeled using the LCAO-type pseudostates described in Sec. III below. Given the impact parameter b and the collision energy E, the coupled equations (7) were integrated in the nuclear $\hat{Z}$ direction starting from a negative point Z_0^- with the initial adiabatic amplitudes describing ground-state hydrogen atom, namely [36,37],

$$a_\alpha^\nu(Z_0^-,b,E)=\exp[-iV_H^{-1}U_{1s}^H Z_0^-]\delta_{H,\nu}\delta_{2p\sigma,\alpha}. \quad (12)$$

The initial point $Z_0^-=50$ bohrs ensured that the $2p\sigma$ orbital is sufficiently decoupled over the range of impact parameters explored. All propagations terminated at the positive coordinate $Z_0^+=400$ bohrs, where the multichannel propagator (8) practically reached its constant asymptotic form, defined [36,37] by the final arrangement probabilities and the residual asymptotic couplings (see below) among the basis states. Since the total ionization probability was nearly constant for $R\geqslant 50$ bohrs, only the bound-electron coupled equations were integrated beyond $R=70$ bohrs. In the range of internuclear separations from 80 to 400 bohrs the propagation could be taken to be block diagonal in the charge exchange channels without a meaningful loss of accuracy [36].

Due to finite residual asymptotic couplings [14,36,37,42–45,64], the final multichannel propagator $G^\infty(b,E)=G(Z_0^+,b,E)$ is generally coupling adiabatic states from the same rearrangement channel. For $Z>Z_0^+$ the propagated amplitudes $\{a_\alpha\}$ therefore oscillate indefinitely [14,37] within each arrangement block. These oscillations reflect the fact that whenever electronic probability is transferred from the target species to the projectile nucleus and/or the ionization continuum, the asymptotic ''probabilistic'' electron must be traveling in *any* two-fragment Jacobi coordinates chosen to describe the system [36,37]. In other words, the propagated amplitudes of one species contain a superfluous traveling phase associated with the fact that part (in the probability sense) of the electron actually belongs to another species. This traveling phase can be eliminated by applying a traveling interaction picture, leading to the following formula for final inertial excitation ($\nu=H$) or state capture ($\nu=He^+$) probabilities [36,37]:

$$W[\phi_{nlm}^\nu \leftarrow \phi_{1s}^H;b,E]=\left|\sum_{\alpha,\beta,\gamma\in\nu}\langle\alpha|nlm\rangle y_{\alpha,\gamma}^* \times\exp[+i\eta_\gamma Z_0^+]y_{\beta,\gamma}^* a_\beta^\nu(Z_0^+,b,E)\right|^2. \quad (13)$$

Here $\{\eta_\gamma\}$ are the eigenvalues of the asymptotic limit $G^\infty(b,E)$ [36,37] of the multichannel propagator (8), $\{y_{\alpha,\gamma}\}$ are the expansion coefficients of the corresponding eigenvectors in the asymptotic adiabatic basis $\{\psi_\alpha(R\to\infty)\}$, and $\langle\alpha|nlm\rangle$ are Stark expansion coefficients [see Eq. (5)]. Unlike the absolute magnitude of the propagated amplitudes $\{a_\alpha^\nu\}$, the probabilities (13) reach constant values at large positive Z [37]. Thus the corresponding state-to-state cross section is the usual semiclassical formula [38,39,43–45]

$$\sigma_{nlm}^\nu(E)=2\pi\int W[\phi_{nlm}^\nu\leftarrow\phi_{1s}^H;b,E]b\,db, \quad (14)$$

from which total and level-selective cross sections are readily obtained.

Because L^2 electronic functions must vanish as $r\to\infty$, the propagated pseudostate probabilities $\{|a_\alpha^I(Z,b,E)|^2\}$ are meaningless as separate entities. However, the sum of these probabilities is a physically meaningful quantity, which for large positive Z must reach some constant fraction [14,36] representing the total ionization probability. The propagation (7) therefore provides the collisional ionization cross section σ^I of ground-state hydrogen upon integrating the pseudospace probability

$$W[I\leftarrow\phi_{1s}^H;b,E]=\sum_{\alpha\in I}|a_\alpha^I(Z_0^+,b,E)|^2 \quad (15)$$

over the impact-parameter range.

III. PSEUDOIONIZATION ORBITALS IN THE LCAO FRAMEWORK

In previous work [36], multichannel PSS simulations of the charge-exchange reaction $H+He^{2+}\to H^++He^+$ were performed with as many as 45 magnetic-even molecular orbitals accurately computed in spheroidal coordinates [47,48]. To describe a particular PSS basis we adopt the notation $\dim\{\psi_\alpha^{He}\}/\dim\{\psi_\alpha^{H}\}/\dim\{\psi_\alpha^{I}\}$, which provides the number of orbitals the basis has from each arrangement subspace (and thus its content, as counting is from the lowest-energy state of a subset). Calculations with the 45-state basis 35/10/0 (denoted 35/10 in Ref. [36]) correctly describe the rising of the measured [2,5] charge-exchange cross section with increasing velocity, but overestimate the peak plateau and the high-energy falloff wing where experiments [6,8] indicate that collisional ionization is significant (see Sec. IV).

In the present multichannel PSS study, the exact 45 HeH^{2+} orbital basis is augmented with pseudoionization states that are linear combinations of Gaussian basis functions. This choice is motivated by the existing efficient techniques [65] for analytic calculation of dynamical couplings when the adiabatic states are expanded in the Cartesian Gaussians

TABLE I. Gaussian basis functions.

Center	Type[a]	Exponents
He	s	2200.0,730.0,243.0,81.0,27.0,9.0,3.5,
		1.6,0.7,0.32,0.15,0.07,0.032,0.015,0.007
	p	30.0,12.0,5.0,2.0,0.9,0.4,
		0.19,0.09,0.04,0.019,0.09
	d	7.0,1.4,0.4,0.15,0.07,0.033,0.015
	f	1.0,0.4,0.17,0.055,0.02
	g	0.085,0.03
	h	0.045,0.015
H	s[b]	837.22,123.524,27.7042,7.825 99,2.565 04,
		0.938 258,0.372 145,0.155 838,0.066 18,0.022
	p	15.0,3.0,0.8,0.3,0.13,0.06,0.028,0.013
	d	0.5,0.1,0.032,0.015
	f	0.06
CC[c]	s	12.3,5.9,2.86,1.12,0.48,0.22
	p	3.5,2.49,1.79,1.29,0.63,0.29
	d	2.16,0.72,0.24
	f	1.53,0.51

[a]Represents the sum $i+j+k$ of the indices defining the Gaussian (16).
[b]See Ref. [66].
[c]$He^{2+}+H^{+}$ center of charge.

$$g_s(\vec{r}_A)=x^i y^j z^k \exp(-\zeta r_A^2), \tag{16}$$

where $\vec{r}_A$ is the electron position relative to center A (usually a nucleus) and the label s stands for the integer numbers i,j,k and the screening factor ζ. Molecular orbitals and pseudoionization functions are then obtained by solving on a finite Gaussian basis $\{g_s\}$, a generalized eigenvalue equation for the R-dependent electronic Hamiltonian (3).

The first step in solving Eq. (2) on the Gaussian basis is to obtain two mutually uncoupled subsets of zeroth-order molecular orbitals and pseudoionization states. The bound-electron orbitals are expressed as linear combinations of Gaussian functions centered on He^{2+} and H^{+} (Table I), namely,

$$\chi_\alpha(\vec{R},\vec{r})=\sum_{s\in \mathrm{He}} c_{\alpha,s}(R) g_s(\vec{r}+q\vec{R})+\sum_{s\in \mathrm{H}} c_{\alpha,s}(R) g_s(\vec{r}-p\vec{R}), \tag{17}$$

with the coefficients $\{c_{\alpha,s}\}$ satisfying at each R the set of homogeneous equations [67,68]

$$\sum_{t\in \mathrm{He,H}} (\langle g_s|H_{\mathrm{BO}}|g_t\rangle-\langle g_s|g_t\rangle\epsilon_\alpha)c_{\alpha,t}=0, \quad s\in \mathrm{He,H}. \tag{18}$$

Similarly, the zeroth-order pseudoionization orbitals are superpositions of the Gaussians (Table I) whose origin is the center of charge of the nuclei He^{2+} and H^{+} (Sec. II), i.e.,

$$\chi_\alpha(\vec{R},\vec{r})=\sum_{s\in \mathrm{I}} c_{\alpha,s}(R) g_s(\vec{r}+\vec{R}/3). \tag{19}$$

TABLE II. Principal and absolute magnetic numbers and the asymptotic localization atom for the 24 even HeH^{2+} orbitals computed using the LCAO basis of Table I.

Atom	$\lvert m\rvert$	n	HeH^{2+} orbitals[a]
He^{+}	0	1	$1s\sigma$
		2	$3d\sigma,2s\sigma$
		3	$4f\sigma,3p\sigma,3s\sigma$
		4	$6h\sigma,5f\sigma,4p\sigma,4s\sigma$
	1	2	$2p\pi$
		3	$3d\pi,3p\pi$
		4	$5g\pi,4d\pi,4p\pi$
	2	3	$3d\delta$
		4	$4f\delta,4d\delta$
	3	4	$4f\phi$
H	0	1	$2p\sigma$
		2	$5g\sigma,4d\sigma$
	1	2	$4f\pi$

[a]United-atom notation.

Accordingly, the zeroth-order pseudoionization coefficients obey the set

$$\sum_{t\in I} (\langle g_s|H_{\mathrm{BO}}|g_t\rangle-\langle g_s|g_t\rangle\epsilon_\alpha)c_{\alpha,t}=0, \quad s\in \mathrm{I}. \tag{20}$$

Expanding the pseudostates (19) using Gaussians whose origin is at the molecular center of charge is justified by the fact the as $R\to\infty$ the exact adiabatic continuum orbitals have Li^{2+} limits and do not localize on either one of the nuclei (Fig. 1).

With the basis of Table I, the zeroth-order calculation supplied 35 center-of-charge functions and a set of 42 molecular orbitals having negative energies over the R range 0.01–70 bohrs. However, on comparing the LCAO electronic curves with our previous exact calculations [36], only the 24 states listed in Table II were considered accurate enough to participate in the PSS simulations. Only these orbitals (with the exception of $4f\phi$) were allowed to dynamically couple to the pseudoionization states (Sec. IV). The 35 zeroth-order center-of-charge orbitals satisfying Eq. (20) have no physical meaning. At large R they all have positive energies ranging from 0.1 to 50 hartree, as would be anticipated when the kinetic-energy operator is expanded on the center-of-charge Gaussian basis functions.

In the final step of the LCAO pseudostate calculation H_{BO} is mixing the zeroth-order molecular and center-of-charge orbitals. This is accomplished by solving the generalized eigenvalue equation corresponding to the set of homogeneous equations [67,68]

$$\epsilon_\alpha d_{\alpha,\alpha}+\sum_{\beta\in \mathrm{I}} (\langle \chi_\alpha|H_{\mathrm{BO}}|\chi_\beta\rangle-\langle \chi_\alpha|\chi_\beta\rangle U_\alpha)d_{\alpha,\beta}=0,$$

$$\alpha\in \mathrm{He,H}, \tag{21a}$$

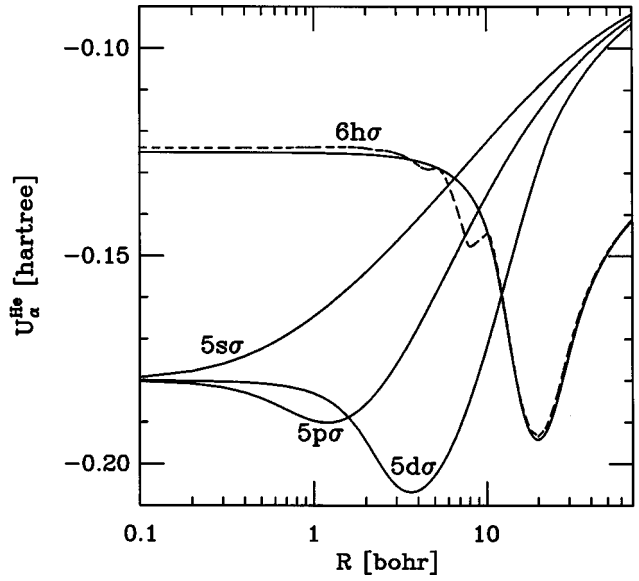

FIG. 2. Exact (solid line) and LCAO (broken line) electronic energy curves of the HeH^{2+} orbital $6h\sigma$. Also shown are three exact σ curves crossing the $6h\sigma$ potential.

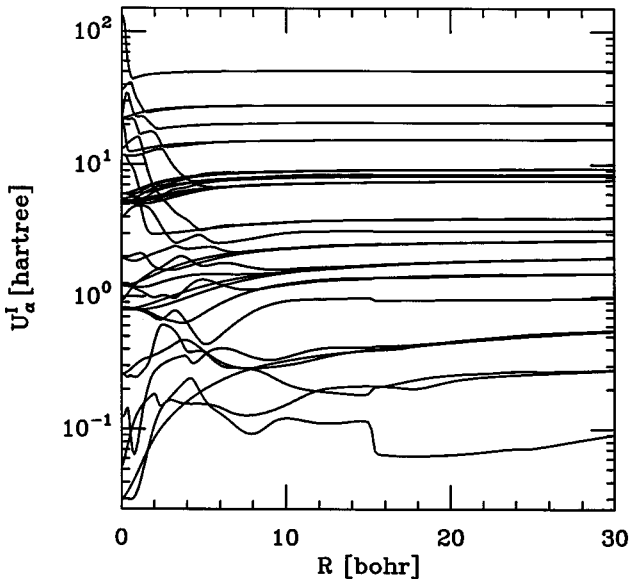

FIG. 3. The 35-LCAO-pseudostate ionization spectrum from $R=0.01$ to 30 bohrs.

$$\epsilon_\alpha d_{\alpha,\alpha}+\sum_{\beta\in \mathrm{He,H}}(\langle\chi_\alpha|H_{\mathrm{BO}}|\chi_\beta\rangle-\langle\chi_\alpha|\chi_\beta\rangle U_\alpha)d_{\alpha,\beta}=0,$$

$$\alpha\in \mathrm{I}. \quad (21b)$$

The solution of the bound-ionization generalized eigenvalue system (21) yields an orthonormal set of molecular and pseudoionization orbitals $\{\psi_\alpha\}$ with energies $\{U_\alpha\}$. The orbitals satisfying Eq. (21) may be expressed as linear combinations of Gaussian functions from three centers,

$$\psi_\alpha(\vec{R},\vec{r})=\sum_{s\in \mathrm{He}} C_{\alpha,s}(R)g_s(\vec{r}+q\vec{R})+\sum_{s\in \mathrm{H}} C_{\alpha,s}(R)$$

$$\times g_s(\vec{r}-p\vec{R})+\sum_{s\in \mathrm{I}} C_{\alpha,s}(R)g_s(\vec{r}+\vec{R}/3) \quad (22)$$

and

$$C_{\alpha,s}(R)=\sum_{\beta\in \mathrm{He,H,I}} d_{\alpha,\beta}(R)c_{\beta,s}(R). \quad (23)$$

The coefficients $\{C_{\alpha,s}\}$ define the generalized eigenfunctions of H_{BO} on the Gaussian basis. We mention here that the zeroth-order basis in Eq. (21) was actually truncated to include just the 42 negative-energy molecular orbitals and the 35 pseudocontinuum functions. This but slightly reduced the numerical accuracy of the final molecular and ionization LCAO orbitals and their coefficients still satisfy the generalized eigenvalue equation within an energy error of less than 10^{-10} hartree over the relevant R range.

The LCAO electronic curves $\{U_\alpha\}$ of the 24 orbitals in Table II are nearly identical to the zeroth-order energies $\{\epsilon_\alpha\}$ throughout the R range 0.01–70 bohrs. Compared with the exact orbital energies [36], these LCAO curves are fairly accurate, with an average discrepancy of less than 0.005%. The poorest agreement is for the $5g\sigma$, $6h\sigma$, and $5g\pi$ energies, which below 3.5 bohrs are about 0.002 hartree above (Fig. 2) the exact curves [36]. For these high united-atom angular-momentum states the basis of Table I, being short on g- and h-type Gaussians, is clearly deficient. Also, between 6 and 10 bohrs, the LCAO orbital identified as $6h\sigma$ is heavily mixed with crossing orbitals (see below) and its energy is lower than the exact values by as much as 0.01 hartree (Fig. 2). Despite this inaccuracy $6h\sigma$ is included in the bound-ionization dynamical calculation so as to have a complete σ subshell interacting with the pseudoionization states. Note that analysis of our previous calculations [36] indicates that $6h\sigma$ is unimportant for capturing the hydrogen electron.

The HeH^{2+} BO electronic system being separable in spheroidal coordinates [46–50] contains numerous same-symmetry (e.g., σ or π) curve crossings (see, e.g., Fig. 2). In the variational LCAO calculation such true crossings appear as avoided crossings, so the curves and the associated dynamical couplings get distorted. The better the basis, the narrower these spurious avoided crossings. With a narrow avoided crossing it is numerically possible to smooth the curves and the dynamical couplings in the vicinity of the crossing and relate them to the correct order of states. This proved to be the case for all the molecular orbitals in Table II, with the exception of $6h\sigma$. The failure here between $R=6$ and 10 bohrs is not due to the $6h\sigma$ deficiency of the basis, but rather to its inability to describe the crossing partners $5s\sigma$ and $5p\sigma$ (Fig. 2). This conclusion was corroborated by examining the dynamical couplings of $6h\sigma$ with other LCAO bound or ionization orbitals, which, albeit somewhat inaccurate, were still rather smooth in this range.

In contradistinction to the molecular orbitals, the LCAO pseudoionization curves $\{U^{\mathrm{I}}_\alpha\}$ and $\{\epsilon_\alpha\}$ are quite different, with the former being positive over the entire (not just the large) R range, as is proper for continuum representing states. The difference between the two energy sets emerges from the requirement [via Eq. (21)] that the pseudoionization and the bound orbitals be mutually orthogonal. Figure 3 provides the 35-state pseudoionization spectrum from $R=0.01$ to 30 bohrs. While at large internuclear separations the

curves are rather constant, they strongly vary below 15 bohrs as do the bound-state electronic energies. Also, several narrow avoided crossing emerged in the calculation. These have been smoothed after switching the order of pseudostates as were the LCAO bound-orbital crossings discussed above. Broad avoided crossings of pseudoionization states are left unaltered, however.

Collisional couplings [Eq. (10)] among the 59 (24 bound-electron and 35 pseudoionization) orbitals have been computed using the analytical method [65]. The LCAO couplings between the 24 bound orbitals of Table II compared favorably with our previous exact results [36]. The PSS simulations reported in the next section employ the exact dynamical couplings [36] between the lowest 45 bound-electron orbitals, the LCAO couplings of the first 23 ($4f\phi$ is not included) orbitals in Table II to the 35 pseudoionization functions, and the LCAO couplings among the latter group. The electronic energy set $\{U_a\}$ correspondingly comprises the 45 exact curves from our previous study [36] and the R-dependent pseudoionization energies shown in Fig. 3. The coupling of $4f\phi$ to the pseudoionization set was ignored because previous results [36] suggest that this orbital hardly participates in the electron transfer reaction.

IV. RESULTS AND DISCUSSION

Multichannel PSS total cross sections for the charge-exchange reaction $H+He^{2+}\rightarrow H^{+}+He^{+}$ and the collisional ionization $H+He^{2+}\rightarrow H^{+}+He^{2+}+e^{-}$, calculated with the basis sets 20/4/35 and 35/10/35, are depicted in Fig. 4 as a function of the collision velocity. For comparison, Fig. 4 also displays our previous [36] multichannel PSS results computed with the basis 35/10/0 (i.e., without pseudoionization states); the 35/10/35 electron-capture cross sections obtained using the single-channel propagator G_{H} (for the incoming arrangement); the experimental charge-exchange [2,5] and ionization [6,8] measurements; and also the translation-factor calculations of Errea *et al.* [30] (adiabatic basis), Fritsch [31] (atomic states), and Winter (triple-center basis) [32], chosen to represent a vast pool [17,18,20,23,25–27,29–32,34] of theoretical results. The 35/10/35 multichannel PSS charge-exchange and ionization cross sections shown in Fig. 4 are provided in Table III, which also includes results for selective capture into energy levels of the helium ion and hydrogen target excitation.

The data portrayed in Fig. 4 corroborate the conclusions drawn from our former simulations [36] performed without pseudoionization orbitals. First of all, notice that the single-channel propagator G_{H} [Eqs. (10) and (11)] underestimates the charge-exchange cross section and its deficiency is increasing with energy. The superiority of the multichannel propagator (8) is even more pronounced here than with a strictly bound-electron PSS basis [36]. We mention in particular that throughout the velocity range 0.25–1.2 a.u., the smaller PSS basis 20/4/35 yields multichannel cross sections of significantly better quality than the 35/10/35 G_{H} results. Overall the convergence with respect to the bound-electron basis size is clearly improved when pseudoionization states participate in the simulation. In fact, only at the falloff wing (from $\sim$0.9 a.u.) do we find a clear discrepancy between the multichannel 20/4/35 and 35/10/35 cross sections, the former

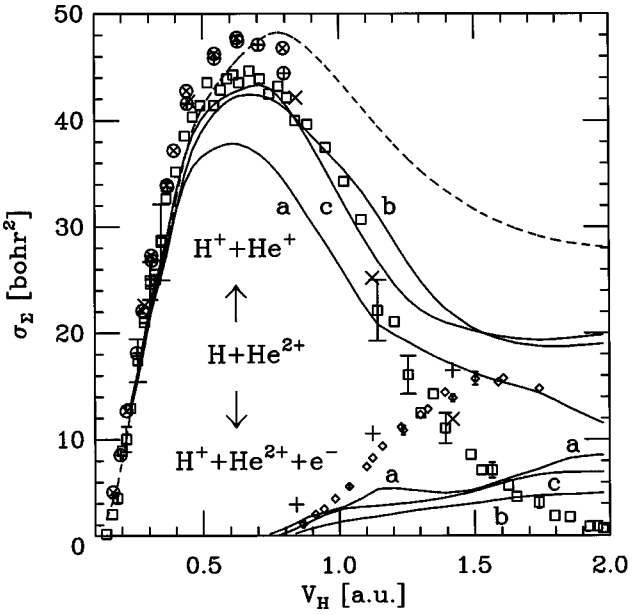

FIG. 4. Cross sections as a function of the target-projectile velocity for the charge-transfer reaction $H(1s)+He^{2+}\rightarrow H^{+}+He^{+}$ and the ionization process $H(1s)+He^{2+}\rightarrow H^{+}+He^{2+}+e^{-}$. The broken curve is the multichannel PSS capture cross section calculated with the strictly bound-state basis 35/10/0 [36]. The solid curves are cross sections computed including 35 pseudoionization states in different PSS models: curve *a*, the target propagator G_{H} defined on the basis 35/10/35; curve *b*, a multichannel propagator (8) for the basis 20/4/35; curve *c*, the 35/10/35 multichannel propagator. The three upper solid curves are calculated charge-transfer cross sections to be compared with the measured points (□) of Shah and Gilbody [2] and Nutt *et al.* [5]. The calculated ionization cross sections are the three lower solid curves and the corresponding experimental data (◇) are from Shah and Gilbody [6] and Shah *et al.* [8]. Error bars at representative points reflect the reported statistical error. The relative systematic errors in the charge-exchange and ionization measurements were estimated at 15% [2] and 5% [8], respectively. Also shown are the charge-transfer (×) and ionization (+) results of Winter [32] and strictly capture cross-section calculations from Errea *et al.* [30] (⊗) and Fritsch [31] (⊕).

being visually higher (Fig. 4, curves *b* and *c*). This behavior indicates that the 35/10/35 charge-exchange calculations are reaching the limit in regard to extending the bound-state part of the PSS basis [36]. Furthermore, notice that below $V_{\mathrm{H}}\approx 0.45$ a.u. the 35/10/0 [36] and the 35/10/35 charge-exchange cross sections are nearly identical, with the inclusion of pseudoionization states causing just a slight increase in the transfer cross section at the beginning of the rising wing. Only above 0.45 a.u. is the capture cross section calculated with pseudoionization states (Fig. 4, curve *c*) becoming progressively lower than our previous [36] 35/10/0 transfer results (Fig. 4, broken curve), which clearly overshoot the experiment. The 35/10/35 simulations reveal that the ionization channel is participating more actively from $\sim$0.45 a.u., which is the velocity where the transfer cross sections with and without ionization functions indeed depart (Fig. 4).

Across the charge-transfer peak and into the falloff wing, up to about $V_{\mathrm{H}}\approx 1.1$ a.u. (30 keV/amu), the simulated 35/10/35 multichannel PSS cross sections are a trifle lower than

TABLE III. Charge exchange, ionization, and level capture and excitation cross sections (in bohr^2) as a function of the target-projectile velocity (in a.u.) for $H(1s)+He^{2+}$ collisions, computed using the multichannel PSS propagator with the 35/10/35 basis described in the text.

V_H	$\sigma_\Sigma^{He^+}$	σ_Σ^{I}	$\sigma_{1s}^{He^+}$	$\sigma_{n=2}^{He^+}$	$\sigma_{n=3}^{He^+}$	$\sigma_{n=4}^{He^+}$	$\sigma_{n=5}^{He^+}$	$\sigma_{n=2}^{H}$	$\sigma_{n=3}^{H}$
0.2313	13.2286	0.0051	0.0332	11.9322	1.0515	0.1672	0.0445	0.1540	0.0168
0.2586	16.4096	0.0062	0.0490	14.3723	1.6498	0.2593	0.0792	0.2564	0.0337
0.2833	19.7105	0.0113	0.0704	16.8290	2.3023	0.3927	0.1161	0.4570	0.0572
0.3060	22.7924	0.0163	0.0915	19.1887	2.8403	0.5298	0.1421	0.5028	0.0698
0.3271	24.9301	0.0209	0.1092	20.8755	3.1424	0.6362	0.1668	0.4870	0.0786
0.3469	26.8164	0.0250	0.1245	22.3995	3.3529	0.7346	0.2048	0.5271	0.0948
0.3657	28.9062	0.0287	0.1395	24.0348	3.6326	0.8417	0.2577	0.6269	0.1196
0.4006	33.2389	0.0462	0.1646	27.2047	4.3787	1.1008	0.3900	0.9530	0.2175
0.4327	36.5526	0.0816	0.1867	29.1431	5.2829	1.3819	0.5580	1.2419	0.3779
0.4626	38.6462	0.1003	0.1997	29.8356	6.2198	1.6760	0.7151	1.4007	0.5194
0.4906	39.9460	0.1127	0.2161	29.9290	7.0044	1.9690	0.8276	1.5720	0.6036
0.5172	40.8643	0.1177	0.2334	29.8440	7.6309	2.2509	0.9051	1.8192	0.6307
0.5424	41.4839	0.1450	0.2449	29.6493	8.0688	2.5478	0.9732	2.1556	0.6337
0.5897	42.3290	0.2405	0.2987	29.3491	8.4257	3.0855	1.1701	2.7753	0.6481
0.6334	42.8346	0.3295	0.3620	29.1735	8.2636	3.5852	1.4503	3.2426	0.7637
0.7082	43.3488	0.6026	0.5293	29.0066	7.5651	4.2056	2.0422	3.5699	1.0233
0.7423	43.0262	0.7813	0.6223	28.4216	7.1401	4.4515	2.3908	3.7351	1.0466
0.7758	42.2772	1.0267	0.7172	27.3581	6.7795	4.6639	2.7585	3.8974	1.0870
0.8070	41.3058	1.3211	0.8216	26.0876	6.4873	4.8120	3.0972	4.0358	1.1796
0.8379	40.1734	1.6631	0.9213	24.7362	6.2140	4.9050	3.3969	4.1467	1.3209
0.8815	38.3937	2.1909	1.0847	22.7492	5.8450	4.9807	3.7341	4.2601	1.5697
0.9501	35.3186	3.0043	1.3611	19.6425	5.2745	4.9561	4.0845	4.3617	1.9920
1.0181	32.1231	3.5444	1.6507	16.7678	4.7105	4.7278	4.2664	4.4467	2.3586
1.0817	29.2694	3.7000	1.8495	14.2890	4.2634	4.5185	4.3490	4.6908	2.5755
1.1419	26.8104	3.7924	1.9627	12.1257	3.8866	4.3972	4.4381	5.1439	2.6846
1.2046	24.5896	3.9379	2.0056	10.1549	3.5384	4.2854	4.6052	5.8124	2.7926

the experiment. This observation suggests that 45 bound-electron orbitals are sufficient for a good, yet not a complete, description of the transfer reaction. It is indeed an encouraging outcome regarding the reliability of multichannel PSS calculations, as higher He^+ states not included in the basis should conceivably play some small supporting role in the capture of the electron from hydrogen atom. Evidence to that effect is inferred below from the level-selective cross sections. The salient feature emerging from Fig. 4 is that the multichannel PSS curve *c* reproduces the charge-exchange cross section until about 1.1 a.u., where it begins to deviate away from the measurements in faster collisions, a behavior synchronous with the multichannel 35/10/35 ionization cross sections, which in the range 0.65–0.95 a.u. conform with experiment [6,8] while increasingly underestimating it above $\sim$1 a.u. (Fig. 4), most likely because the LCAO pseudocontinuum set is of inherently limited quality. Note that up to $V_H \approx 1.1$ a.u. the 35/10/35 charge-exchange cross sections are of accuracy comparable to the translation-factor results of Winter [32].

On the one hand, the agreement existing below $V_H \sim 0.45$ a.u. between the charge-exchange curves calculated with and without ionization representing orbitals and, on the other hand, the fact that curve *c* reproduces the measured cross section above this point and well into the falloff wing, concurrently with a correct description of ionization in this range, validate the accuracy of the multichannel PSS approach [37]. We now turn to discuss quantitative details of the charge-exchange mechanism, namely, the level breakup of the results and its experimental manifestation.

A. Level-selective capture: $H(1s)+He^{2+} \rightarrow H^+ + He^+(n)$

Our previous 35/10/0 multichannel simulations of the $H(1s)+He^{2+}$ collision [36] revealed a mechanism for electron capture characterized by pronounced transfer ($\sim$25%) into He^+ levels higher than $n=2$. In comparison, semiclassical calculations employing either asymptotic atomic [17,18,23,25,26,31,32,34] or adiabatic molecular [20,27,29,30] basis functions modified by electron translation factors predict, for the $n \geqslant 3$ levels, a rather diminished transfer role ($\sim$5%). The present extended basis simulations conform with the mechanism that emerged from our strictly bound-electron multichannel PSS study [36].

Figures 5 and 6 depict the 35/10/35 (solid curves) and 35/10/0 (broken curves) cross sections for selective capture by five He^+ energy levels up to $V_H \approx 1.1$ a.u. (the range where $\sigma_\Sigma^{He^+}$ is accurate; see Fig. 4). To demonstrate the convergence pace, the figures also include representative 20/4/35 level-selective cross sections. Inspecting the partial cross sections, it is seen that excluding transfer into the ground-state $He^+(1s)$, $\sigma_n^{He^+}$ generally decreases with *n* and its peak shifts to higher velocities. These trends suggest that

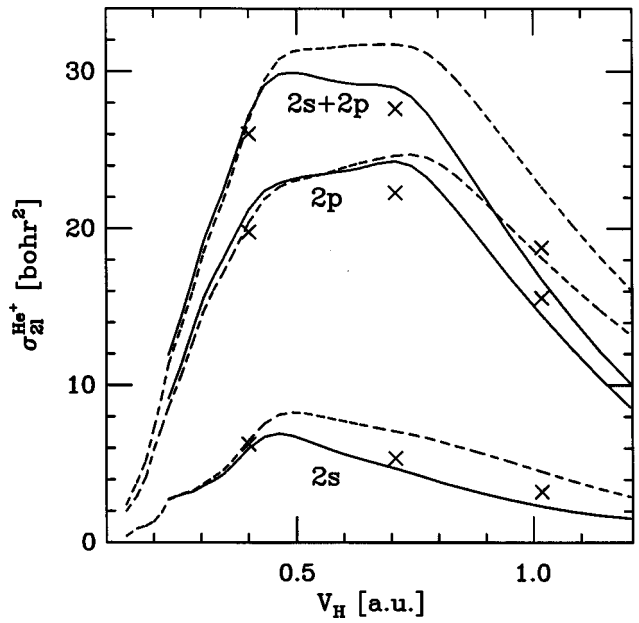

FIG. 5. Multichannel propagator cross sections for the partial electron transfer reactions $H(1s)+He^{2+}\rightarrow H^+ + He^+(2l)$ as a function of the target-projectile velocity, calculated with the 35/10/35 (solid lines) and the 35/10/0 (broken lines) PSS basis sets. The curves $2s$ are the cross sections for capture by $He^+(2s)$; $2p$ labels the curves for transfer into $He^+(2p)$; curves $2s+2p$ represent the total capture by the level $n=2$ of helium ion. Three 20/4/35 points ($\times$) are also shown for each partial cross section to illustrate the convergence quality.

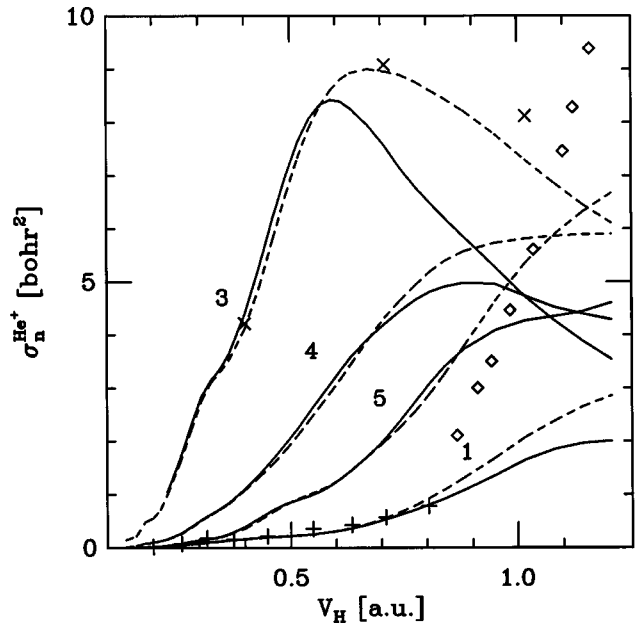

FIG. 6. Multichannel 35/10/35 (solid lines) and 35/10/0 (broken lines) PSS cross sections for selective electron transfer $H(1s)+He^{2+}\rightarrow H^+ + He^+(n)$, as a function of the target-projectile velocity. The principal He^+ quantum number labels the transfer curves. Three representative 20/4/35 points ($\times$) of $\sigma_3^{He^+}$ are depicted. Also shown are experimental total ionization points ($\diamond$) from Fig. 4 and capture cross sections ($+$) into $He^+(n=3)$ calculated by Fritsch [31].

the He^+ levels are mainly populated by direct capture from the incoming state $2p\sigma$.

Inferring from a simple 2×2 model we surmise that efficient transitions occur when the coupling of the states involved is comparable to their energy difference. The transition probability is attenuated, on the other hand, if the coupling is either smaller or larger relative to the energy gap. Hence follow the convex transfer shapes (e.g., Fig. 5) as collisional couplings increase linearly with the velocity while energy differences remain constant [Eq. (10)]. Notice that the larger the n, the wider the gaps separating the curve $U_{2p\sigma}$ from the electronic-energy curves dissociating to the level n of the helium ion. This explains why the maximum transfer shifts to higher velocity for larger n. Moreover, dynamical couplings usually decrease as Δn increases [36], so large n generally means weaker couplings with the initial electron state $2p\sigma$, and therefore $\sigma_n^{He^+}$ is expected to decrease with n. Qualitatively, collisional ionization may be considered as capture into the highest shell. Thus the ionization cross section should peak the farthest with its rising wing initially being a lower bound to He^+ excited-level capture, as is indeed demonstrated in Fig. 6 by the experimental ionization points.

The exceptionally low capture by $He^+(1s)$ (curves 1, Fig. 6) is actually not at all surprising. First notice that $U_{2p\sigma}(R)-U_{1s\sigma}(R)>|U_{2p\sigma}(R)|$ for $R\in[0,\infty)$, so the transfer peak should appear at velocities where ionization is already prominent. Second, because $1s\sigma$ is a highly compact state, its coupling (10) to $2p\sigma$ is significant (with a maximum of 0.5 bohr^{-1}) only below 2 bohrs, where $U_{2p\sigma}(R)-U_{1s\sigma}(R)\approx 3.5$ hartree. These facts imply that in the range below $V_H\approx 1.1$ a.u., $\sigma_{1s}^{He^+}$ is a lower bound of partial transfer cross sections. Accordingly, cross sections for capture by all the helium ion levels with $n>5$ should at most be a trifle higher than the $n=1$ curve, say, maximum 1 bohr^2 at the charge-transfer peak plateau. Thus we would expect a reliable simulation with only 35 states from $\{\psi_{He}\}$ to yield a theoretical $\sigma_{\Sigma}^{He^+}$ that is somewhat lower than the experimental results (see Fig. 4).

It is interesting to note that translation-factor simulations paint a rather different picture of level-selective capture. Both PSS [20,27,29,30] and atomic-state [17,18,23,26,31,32,34] calculations generally predict that about 95% of the peak transfer is into $He^+(n=2)$ (see Fig. 8 in Ref. [36]), regardless of the number of higher-level basis functions employed. For comparison, the multichannel PSS results suggest $\sim$75% capture by the dominant level, and at the reaction peak the cross sections are converged (Figs. 4–6) only when the basis includes higher helium-ion and ionization states [36]. The reason for the diminished transfer role of He^+ levels higher than $n=2$ is that the capture matrix elements between translation-factor modified states are in fact attenuated. The modified $He^+(n=2)$ level, which in the atomic-state expansion method is actually degenerate with the hydrogen ground state, then necessarily becomes transfer prominent. For instance, the charge exchange into He^+ $(n=4)$ from atomic-state translation-factor simulations [31] is as low as the capture by the ground-state helium ion or the ionization current (see Fig. 6). In contrast, the multichannel PSS calculations predict a gradual decrease in the partial transfer cross section from the main participant level down to

ionization and the energetically remote ground state of the helium ion (Figs. 5 and 6).

Comparing the 35/10/35 and 35/10/0 results, it is seen that the main effect of concurrent ionization is to increasingly (with V_H) attenuate the partial transfer cross sections, beginning shortly before the peak of the corresponding 35/10/0 curves (Fig. 6). However, participating ionization states also influence the lower-velocity branch of $\sigma_n^{He^+}$, where the multichannel PSS simulation with pseudostates yields slightly elevated total and partial capture cross sections (Figs. 4–6). Similar findings emerge on comparing the current and the previous [36] single-channel propagator G_H results. It is rather interesting that including pseudoionization orbitals affects simulations below $V_H=0.5$ a.u., where the total ionization cross section is less than 0.1 bohr^2 (Table III) and probably undetectable experimentally. Even after the measured ionization threshold [6,8], the attenuation of the level-selective and the total transfer cross sections greatly exceeds the magnitude of the multichannel ionization cross section itself (Fig. 4). These observations are consistent with the fact that the exclusion of ionization representing states from the close-coupling set introduces a ''wall effect'' to the simulation [45], albeit a rather soft one below the ionization threshold.

B. Postcollision emission cross sections

The level-selective cross sections $\sigma_n^{He^+}$ and $\sigma_{nl}^{He^+}$ are identifying characteristics of the charge-transfer mechanism, which, unlike the total capture cross section, experimentally are only indirectly accessible through the fluorescence intensities from excited species formed in the collision. Similarly, the related target excitation cross sections σ_n^H and σ_{nl}^H must be inferred from hydrogen fluorescence after the collision. Hence, to extract reliable partial level cross sections [7,10–13], the collected emission data need to be complete in regard to both cascade contributions and polarization effects [69,70]. Since the slowest reactive He^{2+} on H event terminates after about 0.1 ps [36], whereas lifetimes of excited electronic states are on the nanosecond scale, it should be possible to predict the products emission from theoretical simulation results. Again, care must be exercised to account for cascade contributions [36] and intensity variation due to radiation anisotropy [11,69,70].

Collision products generally radiate anisotropically [69,70]. The reason has to do with the fact that collisions do not necessarily prepare an isotropic distribution of nascent species. The polarization of the emitted radiation may influence the detected intensity [11,70] and, consequently, the reactive cross sections inferred from it. If σ_λ is the total cross section for emitting a photon of wavelength λ by a product species moving in the $\hat{Z}$ direction, then the cross section actually measured at an angle Θ to the incoming beam is given by [70]

$$\overline{\sigma_\lambda}(\Theta)=\frac{3\sigma_\lambda(1-\cos^2\Theta)}{3-P}, \tag{24}$$

where P is the polarization degree

$$P=\frac{\sigma_{\lambda,z}-(\sigma_{\lambda,x}+\sigma_{\lambda,y})/2}{\sigma_{\lambda,z}+(\sigma_{\lambda,x}+\sigma_{\lambda,y})/2}. \tag{25}$$

Here $\sigma_{\lambda,z}$, $\sigma_{\lambda,x}$, and $\sigma_{\lambda,y}$ are the total cross sections for λ photon emissions linearly polarized along the three Cartesian axes of the electronic body-fixed frame. Choosing the body frame as in Sec. II, $\sigma_{\lambda,z}$ and $(\sigma_{\lambda,x}+\sigma_{\lambda,y})/2$ form, respectively, the laboratory-frame cross sections for fluorescence polarized parallel and perpendicular to the plane defined by the beam and the direction of observation. The $\frac{1}{2}$factor in the perpendicular term emerges after averaging the intensity over the azimuthal angle. It is clear from Eq. (25) that the anisotropy of the radiation is a consequence of the collision created ensemble of nascent species. The measured emission cross section $\overline{\sigma_\lambda}$ is generally different from σ_λ, unless the observation is made at the magic angle of 54.7°, where the two quantities coincide [11,70].

The body-frame emission cross sections are uniquely determined from the state-specific reactive cross sections and the fluorescence probabilities (including cascades) of the free product species. For a transfer product helium ion or a collisionally excited hydrogen atom we have, assuming independent level decay [36],

$$\sigma_{\lambda,i}^j(E)=\sum_{n,l,m}\sigma_{nlm}^j(E)P_{\lambda,i}^j(n,l,m),\quad i=x,y,z,\quad j=He^+,H, \tag{26}$$

where E is the scattering energy and $P_{\lambda,i}^j(n,l,m)$ is the probability that the state ϕ_{nlm}^j ($j=He^+$ or H) will procure a photon of wavelength λ linearly polarized in the body-fixed direction $\hat{\imath}$. Photon procuring means that the state will produce the photon either by directly emitting it or via emission further down a decay cascade involving lower states. The state photon procuring probabilities are readily obtained from the decay branching ratios of the excited states, which for He^+ are known analytically [71]. The summation in Eq. (26) is performed over spatial, not the fine-structure [11,69], states of the helium-ion (or hydrogen atom) because the eikonal simulations are conducted without considering the electron spin [14–36]. This is justified by the fact that the high-energy charge-exchange collisions are governed by the Coulombic force. As the radiation-matter coupling here involves the electric dipole, the electron spin is conserved in emission. Hence Eq. (26) would lead to the correct fluorescence cross sections if we surmise that the spin state remains unaltered in the collision (which is the eikonal assumption in the first place).

C. He II Lyman emissions of the captured electron

Figures 7 and 8 juxtapose the 35/10/35, 20/4/35, and 35/10/0 multichannel PSS predictions with the experimental [7,11] cross sections for Lyman fluorescence lines emitted by heliums ion produced in $H+He^{2+}$ charge-exchange collisions. Figure 7 also depicts the measured [2] and the calculated Lyman-α fluorescence induced by electric-field quenching of the metastable $He^+(2s)$ product. Both the spontaneous $(2p)$ and the quenched $(2s)$ Lyman emissions were experimentally detected [2,7,11] perpendicular to the helium ion beam.

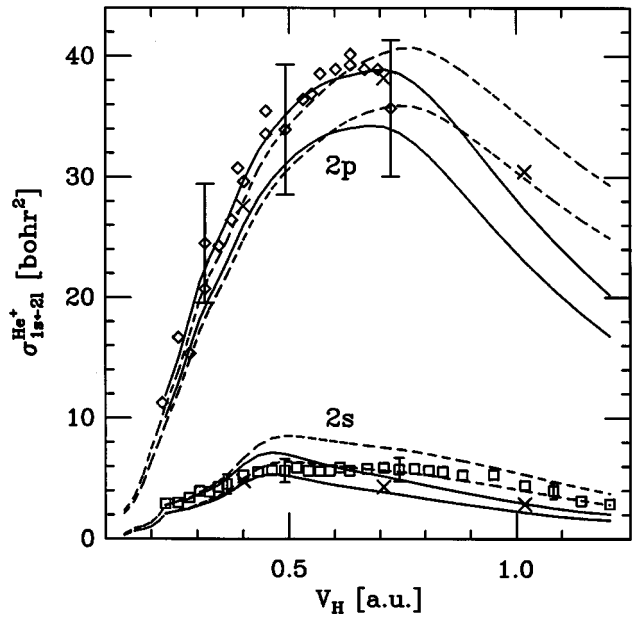

FIG. 7. Cross sections for Lyman-α emissions from the helium ion produced in $H(1s)+He^{2+}$ collisions, displayed as a function of the target-projectile velocity. Two sets of theoretical cross sections were calculated as explained in the text from the multichannel PSS simulation results for the 35/10/35 basis with pseudoionization states (solid lines) and the strictly bound basis 35/10/0 (broken lines). The four calculated cross sections labeled $2p$ are for the $1s\leftarrow 2p$ emission detected at 90° (upper two curves) and 54.7° (lower two curves) with respect to the beam of the nascent capture product. The four curves labeled $2s$ are the radiation cross sections from long-lived metastable helium ions moving in a beam perpendicular to a quenching electric field. The magic-angle and perpendicular $2s$ signals are, respectively, the upper and lower emissions calculated for each PSS set (35/10/35 and 35/10/0). Also shown (×) are representative points of the 20/4/35 90° spontaneous and electric-field quenched emission cross sections. Experimental cross sections: (□) Shah and Gilbody [2] for 90° Lyman-α fluorescence from the metastable $He^+(2s)$ product quenched in electric field and (◇) Ćirić *et al.* [7] and Hoekstra, de Heer, and Morgenstern [11] for spontaneous postcollision He II Lyman-α emission detected perpendicular to the beam. Error bars reflect the root mean square of the reported statistical and systematic errors.

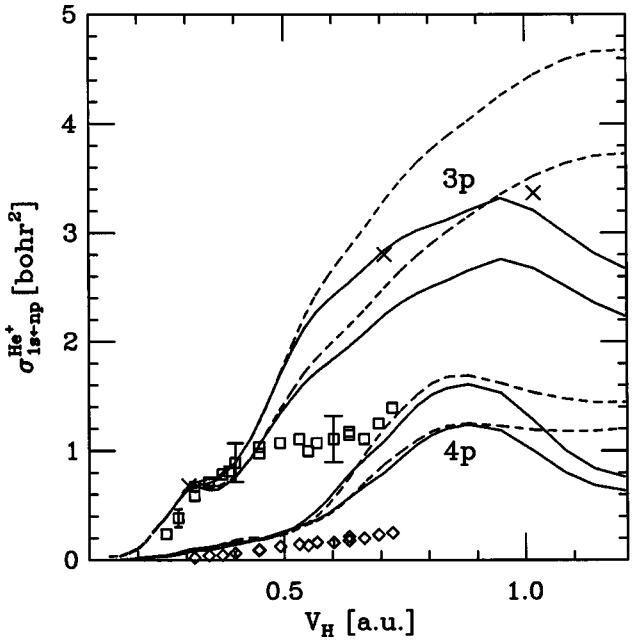

FIG. 8. Calculated cross sections for Lyman-β (upper four curves) and -γ (lower four curves) emissions from the helium ion produced in $H(1s)+He^{2+}$ collisions, as a function of the target-projectile velocity. As with the $1s\leftarrow 2p$ emissions of Fig. 7, the calculated magic-angle $1s\leftarrow 3p$ and $1s\leftarrow 4p$ curves are lower. Also shown are three 20/4/35 cross sections of the $1s\leftarrow 3p$ fluorescence. The experimental data for perpendicular Lyman-β (□) and Lyman-γ (◇) emissions are from Ćirić *et al.* [7] and Hoekstra, de Heer, and Morgenstern [11]. See Fig. 7 for further details.

Comparing Figs. 5 and 7, it becomes evident that in the multichannel PSS model, cascade contributions and polarization effects are important factors determining the spontaneous collision-induced Lyman-α intensities. In contradistinction, translation-factor simulations [17,18,20,23,25–27,29–32,34] essentially reproduce the Lyman-α curve without cascades (see Fig. 11 in Ref. [36]) and place much less emphasis on radiation anisotropy. The reactive 35/10/35 cross section for $He^+(2p)$ production (Fig. 5) generates only 55% of the field-free experimental emission cross sections (Fig. 7). The magic-angle Lyman-α emission lines calculated from the reactive cross sections and theoretical branching ratios using Eq. (26) are roughly 88% of the 90° results. The Lyman-α cross sections perpendicular to the scattering direction calculated with Eqs. (24) and (25) from the aforementioned Cartesian body-frame emission cross sections (26) are in excellent agreement with the experimental points [9,11]. Note that the 20/4/35 smaller-basis simulations provide almost as good agreement with the measurements (Fig. 7). Also, below ~ 0.5 a.u., the 35/10/35 and 35/10/0 spontaneous (and field-induced) Lyman-α emissions are actually quite close, in accordance with the fact that in slow collisions ionization is negligible.

Contrary to the $1s\leftarrow 2p$ fluorescence from the excited product helium ion, the magnitude of the Lyman-α emission induced by quenching the metastable $He^+(2s)$ is only marginally affected by cascade contributions. Relatively few cascades terminate at the $2s$ level as opposed to the number passing through $2p$ en route to the ground state. Thus the magic-angle emission and the reactive capture cross sections are numerically close (within 3%) at $V_H \approx 0.45$ a.u., where the $2s$ transfer peaks. However, in faster collisions the difference widens ($\sim 25\%$ around 1 a.u.) since more excited states participate in the transfer and consequently more cascades decay to the metastable helium ion. Theoretically, the Lyman-α emission induced by a strong perpendicular electric field should have a polarization degree of -1 [2,11]. When the radiation is polarized completely perpendicular to the beam, the observed cross section is 75% of the actual emission (the magic-angle value). The 90° and 54.7° quenched $2s$ emission curves in Fig. 7 therefore represent lower and upper bounds for the observed $2s$ fluorescence (in Ref. [11] the authors estimated $P \approx -0.45$ from the reported strength of the electric field applied in the measurements [2]).

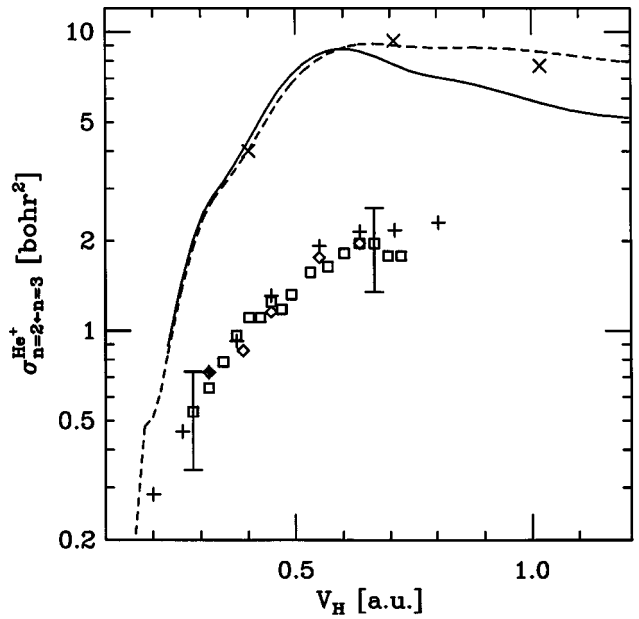

FIG. 9. Multichannel PSS cross sections for He II Balmer-α emission recorded at the magic angle relative to a beam of helium ions produced in $H(1s)+He^{2+}$ collisions, displayed as a function of the target-projectile velocity. Also shown (+) is the emission profile similarly computed using the capture results of Fritsch [11,31]. Experimental cross sections are detected at (◇) 90°, Ćirić *et al.* [7], and (□) 54.7°, Hoekstra, de Heer, and Morgenstern [11]. See Fig. 7 for further details.

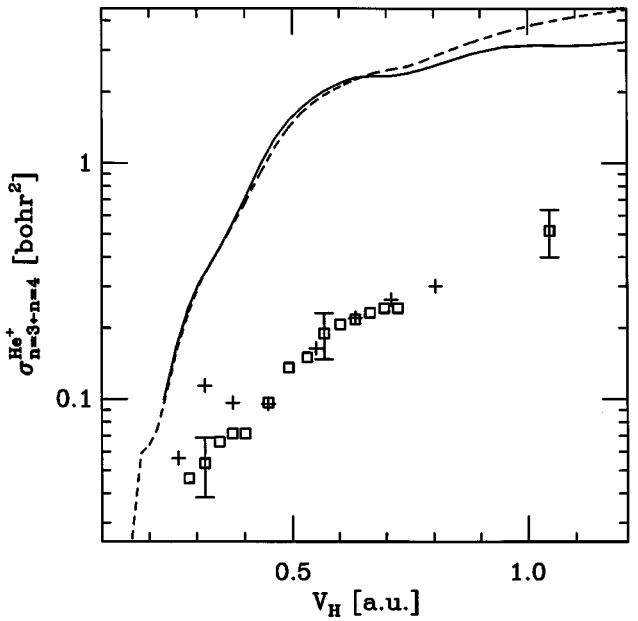

FIG. 10. Multichannel PSS cross sections for Paschen-α emission detected perpendicular to the beam of helium ions produced in $H(1s)+He^{2+}$ collisions, displayed as a function of the target-projectile velocity. Also shown (+) is the emission profile computed from the capture results of Fritsch [11,31]. The experimental cross sections (□) are taken from Hoekstra, de Heer, and Morgenstern [11] and Frieling *et al.* [12]. See Fig. 7 for further details.

The emission bounds computed using the 35/10/35 basis with pseudoionization states correctly describe the Lyman-α cross sections from a field-quenched $He^+(2s)$ product up to about 0.7 a.u., after which they underestimate the measurements [2]. Since the number of cascades ending at the $2s$ metastable terminal rapidly grows with the velocity as discussed above, it is conceivable that if capture levels higher than $n=5$ would have participated in the PSS simulation, the calculated $2s$ Lyman-α line would have been somewhat stronger at the high-velocity end of Fig. 7. This argument applies also to the emissions computed from the 35/10/0 simulations (broken curves), which predict higher bounds for the Lyman-α cross section, primarily because the absence of ionization states increases the capture role of the $He^+(2s)$ orbital (Fig. 5). Notice that in the V_H range 0.4–0.7 a.u., the 35/10/0 perpendicular and magic-angle bounds (Fig. 7) overshoot the field-quenched [2] fluorescence from the metastable helium ion, while above $\sim$0.7 a.u. the 35/10/0 results are rather in good agreement with the measured points. However, for $V_H \geq 0.7$ a.u. the total 35/10/0 cross section [36] and the 35/10/0 prediction for the perpendicularly detected spontaneous Lyman-α line are both clearly in error as opposed to the 35/10/35 calculations (Figs. 4 and 7). So it seems that the 35/10/0 $2s$ results above 0.7 a.u. are fortuitous and the 35/10/35 $2s$ emission bounds are more realistic, especially when considering that for very energetic collisions, cascade contributions are expected to be larger than what a basis of 35 He^+ states provides.

The multichannel PSS predictions for product He^+ Lyman-β and -γ 90° emissions (Fig. 8) agree with the measured cross sections [7,11] up to $V_H \approx 0.45$ a.u., but substantially overshoot the experiment in faster collisions (approximately twice as much at 0.7 a.u.). Notice that like the spontaneous Lyman-α emission (Fig. 7), the Lyman-β and -γ lines are both sensitive to polarization effects that amplify the 90° signal. This means that the sum [7,11,12] of all 90° Lyman intensities (spontaneous and field quenched) may overestimate the peak total charge-exchange cross section by $\sim$10%.

D. He II Balmer-α and Paschen-α emissions of the captured electron

The calculated multichannel PSS and the measured [11] magic-angle Balmer-α emission are compared in Fig. 9. The 35/10/35 cross section for the longer-wavelength Paschen-α line at 90° detection is shown in Fig. 10 together with the experimental results of Hoekstra, de Heer, and Morgenstern [11] and Frieling *et al.* [12]. The multichannel PSS predictions for the Balmer-α and Paschen-α emissions of the captured electron are substantially higher than the measurements. In contradistinction, the emission profiles calculated from the translation-factor results of Fritsch [11,31] are in good agreement with the experimental points (Figs. 9 and 10). The reason why translation-factor emission cross sections are much lower than the multichannel PSS results is that capture by the levels $n \geq 3$ of the helium ion is significantly reduced by the translation-factor modification of the atomic basis states (Sec. IV A).

The exact unmodified dynamical couplings [36] between $2p\sigma$ and the orbitals dissociating to the level $He^+(n=3)$ are actually large in comparison to the separation of the associated electronic-energy curves, thereby leading one to expect the high capture cross sections shown in Fig. 6. Notice that the emitting atomic states are linear combinations [36,46] of

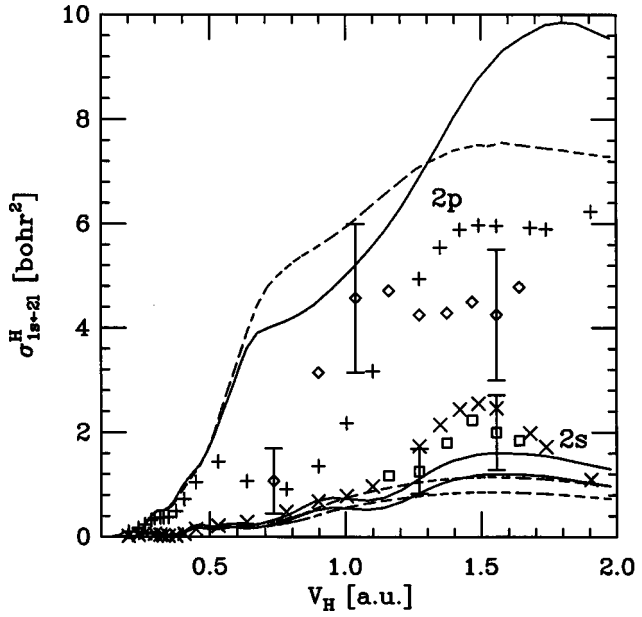

FIG. 11. Cross sections for Lyman-α emission from a hydrogen atom excited by a passing α particle, calculated (see the text) as a function of the relative velocity using the 35/10/35 (solid lines) and 35/10/0 (broken lines) multichannel propagator simulation results and including higher-level cascade contributions. The two $2p$ curves are the magic-angle $1s\leftarrow 2p$ field-free emission. The two 35/10/35 and two 35/10/0 curves labeled $2s$ represent the upper (magic angle) and lower (perpendicular detection) bounds for emission from product metastable hydrogen quenched by a 90° electric field. Also shown are the H($2p$) and H($2s$) emission cross sections computed using the theoretical excitation data provided by Fritsch, Shingal, and Lin [34]. Experimental magic-angle measurements (with the rms error bars as in Fig. 7) are taken from Hughes, Geddes, and Gilbody [13]: (□) H($2s$) and (◇) H($2p$).

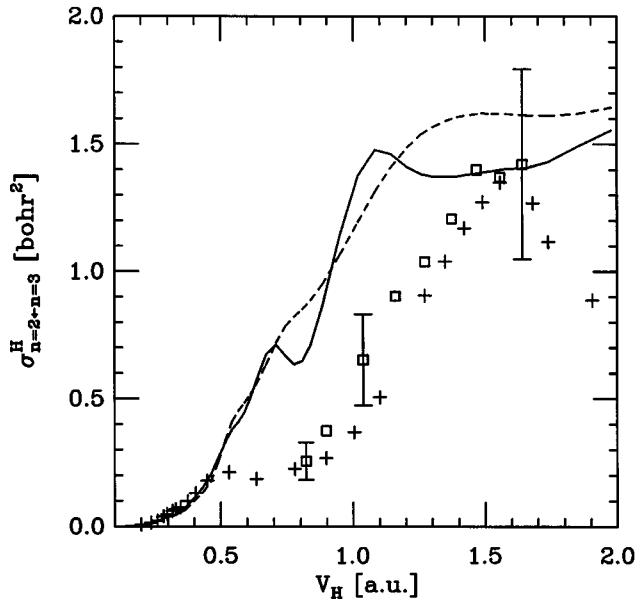

FIG. 12. Calculated cross sections for Balmer-α emission from a hydrogen atom excited by a passing α particle, calculated as a function of the relative velocity. Also shown are emission cross sections (+) predicted from the results of Fritsch, Shingal, and Lin [34] and the magic-angle measurements (□) of Donnelley, Geddes, and Gilbody [10]. See Fig. 11 for further details.

the asymptotic adiabatic states [see Eq. (15)], so that excessive capture by $He^+(n=3)$ related adiabatic orbitals should be reflected also in the Lyman-β line. Yet, up to $V_H \approx 0.45$ a.u., the multichannel PSS prediction for the Lyman-β fluorescence of the captured electron (Fig. 8) is in good agreement with experiment [9,11]. The corresponding Balmer-α emission, however, is approximately thrice higher than the measurements [11] at $V_H = 0.4$ a.u. (Fig. 9). A similar scenario is observed between the Paschen-α and Lyman-γ emissions of He II (Figs. 8 and 10).

In our previous study [36] we conjectured that the discrepancy between the experiment and the multichannel PSS results for the Balmer-α emission (Fig. 9) might be accounted for when optical interference effects are considered. On second thought, this explanation seems to us unlikely because the eventual decay of a highly populated $n=3$ level of He^+ must necessarily procure either a Balmer-α or Lyman-β photon. That is, any interference would at most shift intensities between these lines, but will not attenuate the combined emission cross section. Examining possible wave-packet interferences within the scheme suggested previously [36], we found interference effects to be sufficiently small, so that the independent decay model (Sec. IV B) is reasonably accurate. The multichannel PSS simulations indicate that it is precisely the He^+ Balmer-α emission that is feeding the downstream Lyman-α line up to the experimental value and it should therefore be of comparable intensity (Figs. 5 and 7). At this point we cannot explain the discrepancies from experiment in Figs. 9 and 10.

E. Lyman-α and Balmer-α emissions of the excited hydrogen target

Figures 11 and 12 depict the Lyman-α and Balmer-α emissions from the collisionally excited hydrogen calculated using the 35/10/35 and 35/10/0 simulation results. Although the hydrogen side of the PSS basis is over three times smaller than the He^+-related subspace, the calculated hydrogen emission cross sections are, nevertheless, in rather decent agreement (Figs. 11 and 12) with the experiments [10,13] and other semiclassical calculations [34]. The 35/10/35 hydrogen Lyman- and Balmer-α cross sections are slightly higher (~ 1 bohr^2) than the experimental values obtained at velocities above 0.7 a.u., but are conceivably within the experimental error (Figs. 11 and 12). Considering that the 35/10/35 basis extends only through the level H($n=3$) and the fact that the inclusion of additional levels in the simulation generally decreases the partial cross sections for lower levels [36], we believe that the current PSS results provide a reasonable description of collisional hydrogen excitation. Nevertheless, it is also clear [36] that expanding $\{\psi^H_\alpha\}$ (as well as $\{\psi^{He}_\alpha\}$) should yield an improved picture of the inelastic channel.

V. SUMMARY

The collision system $H+He^{2+}$ has been studied within a multichannel PSS framework [37] that here is extended to include LCAO-type pseudo-orbitals representing the ionization arrangement. The cross section for the charge-exchange

reaction $H(1s)+He^{2+}\rightarrow H^{+}+He^{+}$ calculated with our largest PSS basis 35/10/35 agrees with the measurements [2,5] throughout the transfer peak and well into the falloff wing up to the $\sim$1.1 a.u. (30 keV/amu) center-of-mass velocity. The experimental cross section for the competing collisional ionization process $H(1s)+He^{2+}\rightarrow H^{+}+He^{2+}+e^{-}$ [6,8] is accurately reproduced from its onset to about 1 a.u. with the same basis. The rising wing of the charge-exchange cross section that lies below the ionization threshold is also equally well described by our previous multichannel calculations [36] that employ a 35/10/0 PSS basis without pseudoionization states. These results validate the multichannel approach [37] when unmodified molecular orbitals are employed and particularly because the single-channel (G_{H}) 35/10/35 and 35/10/0 models yield highly deficient descriptions of the charge-exchange reaction.

Our prior [36] and current multichannel PSS simulations of the $H(1s)+He^{2+}$ collision system both determine that $\sim$25% of the charge-transfer peak current flows into He^{+} levels lying above $n=2$. This is 5 times the prediction for $n>2$ capture by semiclassical calculations using basis functions modified with translation factors [17,18,20,25–27,29–32,34]. Although neither state- nor level-selective collision cross sections are directly measurable, they determine the ensuing fluorescence of the collision reactive and excitation products. The cross sections for spontaneous [7,11] and electric-field quenched [2] Lyman-α emissions of the captured electron measured perpendicular to the beam are accurately reproduced from our 35/10/35 multichannel partial capture cross sections $\sigma_{nl}^{He^{+}}$ and the known [71] He II branching ratios. The multichannel calculations are also in reasonable agreement with the 54.7° Lyman-α [13] and 90° Balmer-α [10] fluorescence intensities from the collisionally excited hydrogen, even though the 35/10/35 basis is of lesser quality for hydrogen. These results reconfirm the accuracy of the multichannel PSS model [37], especially when considering the fact that the calculated spontaneous 90° intensity of the He^{+} product Lyman-α line is highly sensitive to both the polarization degree and cascading contributions and is correctly reproduced (Fig. 7) from our partial 35/10/35 reactive cross sections. In this case, cascades amount to $\sim$33% of the emitted peak intensity, whereas the polarization effect is about 10%. These figures are roughly double the generic values experimenters assume [2,7,10–13].

Prominent cascade feeding of the $He^{+}(n=2)$ level unequivocally implies He II Balmer and Paschen series of overall comparable intensity. This is indeed the prediction of the 35/10/35 multichannel PSS calculations (Figs. 8–10). Experiments [7,11,12], however, yield smaller cross sections for the Balmer-α and Paschen-α fluorescence from the helium ion produced in $H(1s)+He^{2+}$ charge-exchange collisions. Low transfer into levels higher than $He^{+}(n=2)$ is generally predicted by various simulations using basis states modified by several types of translation factors [22,27,29–31,33]. The multichannel PSS model [37] conceptually differs from the former methods in two main points: (i) it defines the final-state amplitudes via a traveling interaction picture and (ii) it introduces channel mixing during the propagation, which in spirit is very similar to the Faddeev approach in stationary rearrangement scattering [52]. The accuracy of the multichannel PSS model depends solely on the size of the unmodified orbital set. It remains to be seen whether a more exact treatment of the ionization manifold would change our conclusions.

ACKNOWLEDGMENTS

This research was made possible, in part, by NSF Grant No. CHE9307489. The author expresses his gratitude to Professor Karl F. Freed for his support.

[1] W. L. Fite, A. C. H. Smith, and R. F. Stebbings, Proc. R. Soc. London, Ser. A **268**, 527 (1962).
[2] M. B. Shah and H. B. Gilbody, J. Phys. B **7**, 256 (1974); **7**, 630 (1974); **11**, 121 (1978).
[3] J. E. Bayfield and G. A. Khayrallah, Phys. Rev. A **12**, 869 (1975).
[4] R. E. Olson, A. Salop, R. A. Phaneuf, and F. W. Meyer, Phys. Rev. A **16**, 1867 (1977).
[5] W. L. Nutt, R. W. McCullough, K. Brady, M. B. Shah, and H. B. Gilbody, J. Phys. B **11**, 1457 (1978).
[6] M. B. Shah and H. B. Gilbody, J. Phys. B **14**, 2361 (1981).
[7] D. Ćirić, D. Dijkkamp, E. Vlieg, and F. J. de Heer, J. Phys. B **18**, 4745 (1985).
[8] M. B. Shah, D. S. Elliott, P. McCallion, and H. B. Gilbody, J. Phys. B **21**, 2455 (1988).
[9] D. Ćirić, R. Hoekstra, F. J. de Heer, and R. Morgenstern, in *Electronic and Atomic Collisions*, edited by H. B. Gilbody, W. R. Newell, F. H. Read, and A. C. H. Smith (Elsevier, Amsterdam, 1988), p. 655.
[10] A. Donnelley, J. Geddes, and H. B. Gilbody, J. Phys. B **24**, 165 (1991).
[11] R. Hoekstra, F. J. de Heer, and R. Morgenstern, J. Phys. B **24**, 4025 (1991).
[12] G. J. Frieling, R. Hoekstra, E. Smulders, W. J. Dickson, A. N. Zinoviev, S. J. Kuppens, and F. J. de Heer, J. Phys. B **25**, 1245 (1992).
[13] M. P. Hughes, J. Geddes, and H. B. Gilbody, J. Phys. B **27**, 1143 (1994).
[14] R. D. Piacentini and A. Salin, J. Phys. B **7**, 1666 (1974); **9**, 563 (1976); **10**, 1515 (1977).
[15] T. G. Winter and N. F. Lane, Phys. Rev. A **17**, 66 (1978).
[16] G. J. Hatton, N. F. Lane, and T. G. Winter, J. Phys. B **12**, L571 (1979).
[17] B. H. Brandsen and C. J. Noble, Phys. Lett. **70A**, 404 (1979); J. Phys. B **14**, 1849 (1981).
[18] B. H. Brandsen, C. W. Newby, and C. J. Noble, J. Phys. B **13**, 4245 (1980).
[19] T. G. Winter and G. J. Hatton, Phys. Rev. A **21**, 793 (1980).
[20] M. Kimura and W. R. Thorson, Phys. Rev. A **24**, 3019 (1981).
[21] D. S. F. Crothers and N. R. Todd, J. Phys. B **14**, 2233 (1981); **14**, 2251 (1981).
[22] L. F. Errea, L. Méndez, and A. Riera, J. Phys. B **15**, 101 (1982).

[23] J. F. Reading, A. L. Ford, and R. L. Becker, J. Phys. B **15**, 625 (1982).
[24] H. J. Lüdde and R. M. Dreizler, J. Phys. B **15**, 2713 (1982).
[25] B. H. Brandsen, C. J. Noble, and J. Chandler, J. Phys. B **16**, 4191 (1983).
[26] W. Fritsch and C. D. Lin, Phys. Rev. A **29**, 3039 (1984).
[27] M. C. van Hemert, E. F. van Dishoeck, J. A. van der Hart, and F. Koike, Phys. Rev. A **31**, 2227 (1985).
[28] C. W. Newby, J. Phys. B **18**, 1781 (1985).
[29] L. F. Errea, J. M. Gómez-Llorente, L. Méndez, and A. Riera, Phys. Rev. A **32**, 2158 (1985); **35**, 4060 (1987).
[30] L. F. Errea, J. M. Gómez-Llorente, L. Méndez, and A. Riera, J. Phys. B **20**, 6089 (1987).
[31] W. Fritsch, Phys. Rev. A **38**, 2664 (1988).
[32] T. G. Winter, Phys. Rev. A **37**, 4656 (1988).
[33] L. F. Errea, J. M. Maidagan, L. Méndez, and A. Riera, J. Phys. B **24**, L387 (1991).
[34] W. Fritsch, R. Shingal, and C. D. Lin, Phys. Rev. A **44**, 5686 (1991).
[35] L. F. Errea, L. Méndez, A. Riera, C. Harel, H. Jouin, and B. Pons, Phys. Rev. A **50**, 418 (1994).
[36] G. Hose, Phys. Rev. A **51**, 2222 (1995).
[37] G. Hose, Phys. Rev. A **51**, 2199 (1995).
[38] R. McCarroll, in *Atomic and Molecular Collision Theory*, edited by F. A. Gianturco (Plenum, New York, 1982), p. 165.
[39] J. B. Delos, Rev. Mod. Phys. **53**, 287 (1981).
[40] B. C. Garett and D. G. Truhlar, in *Theoretical Chemistry: Advances and Perspectives*, edited by D. Hendersen (Academic, New York, 1981), Vol. 6A, p. 215.
[41] G. Hose, Comments At. Mol. Phys. **22**, 307 (1989).
[42] D. R. Bates and R. McCarroll, Proc. R. Soc. London, Ser. A **245**, 175 (1958).
[43] A. Riera and A. Salin, J. Phys. B **9**, 2877 (1976).
[44] J. S. Briggs, Rep. Prog. Phys. **39**, 217 (1976).
[45] W. Fritsch and C. D. Lin, Phys. Rep. **202**, 1 (1991).
[46] J. D. Power, Philos. Trans. R. Soc. London, Ser. A **274**, 663 (1973).
[47] D. R. Bates and T. R. Carson, Proc. R. Soc. London, Ser. A **234**, 207 (1956).
[48] T. G. Winter, M. D. Duncan, and N. F. Lane, J. Phys. B **10**, 285 (1977).
[49] L. I. Ponomarev and L. N. Somov, J. Comput. Phys. **20**, 183 (1976).
[50] J. Rankin and W. R. Thorson, J. Comput. Phys. **32**, 437 (1979).
[51] G. Hose, J. Phys. (France) Colloq. **50**, C1-111 (1989).
[52] A multichannel PSS construction is necessary to ensure unique propagation of the time-dependent electronic wave function in charge-transfer collisions [37]. In this context, the multichannel PSS propagator is analogous to the three-body Faddeev equations in stationary rearrangement scattering (Zh. Eksp. Teor. Fiz. **39**, 1459 (1960) [Sov. Phys. JETP **12**, 1014 (1961)]). In both cases, a unique solution is achieved by permitting the mixing of propagators defined by the asymptotic rearrangement channels (boundary conditions). Other attributes of this analogy are, for example, Eq. (4), which is reminiscent of (but not exactly) channel spaces, or the half factor in Eq. (9), reflecting that the adiabatic ionization set is like the intersection of two asymptotic bases (i.e., arrangements).
[53] D. G. M. Anderson, M. J. Antal, and M. B. McElroy, J. Phys. B **7**, L118 (1974); **14**, 1707 (1981).
[54] R. Shakeshaft, Phys. Rev. A **14**, 1626 (1976); **18**, 1930 (1978).
[55] C. D. Lin, T. G. Winter, and W. Fritsch, Phys. Rev. A **25**, 2395 (1982).
[56] T. G. Winter and C. D. Lin, Phys. Rev. A **29**, 567 (1984); **29**, 3071 (1984); **30**, 3033 (1984).
[57] R. Shingal and C. D. Lin, J. Phys. B **22**, L445 (1989).
[58] K. Gramlich, N. Grün, and W. Scheid, J. Phys. B **22**, 2567 (1989).
[59] N. Toshima, J. Phys. B **27**, L49 (1994); Phys. Rev. A **50**, 3940 (1994).
[60] A. Jain, C. D. Lin, and W. Fritsch, Phys. Rev. A **39**, 1741 (1989).
[61] C. F. Melius and W. A. Goddard, Phys. Rev. A **10**, 1541 (1974).
[62] A. López-Castillo, Phys. Rev. A **53**, 818 (1996).
[63] M. Kimura and C. D. Lin, Phys. Rev. A **31**, 590 (1985).
[64] H. Rosenthal, Phys. Rev. Lett. **27**, 635 (1971).
[65] A. Macias and A. Riera, Phys. Rep. **90**, 301 (1982).
[66] P. Siegbahn and B. Liu, J. Chem. Phys. **68**, 2457 (1978).
[67] C. C. J. Roothaan, Rev. Mod. Phys. **23**, 69 (1951); **32**, 179 (1960).
[68] P. O. Löwdin, Rev. Mod. Phys. **32**, 328 (1960).
[69] I. C. Percival and M. J. Seaton, Philos. Trans. R. Soc. London, Ser. A **251**, 113 (1958).
[70] B. L. Moiseiwitsch and S. J. Smith, Rev. Mod. Phys. **40**, 238 (1968).
[71] H. A. Bethe and E. E. Salpeter, *Quantum Mechanics of One- and Two-Electron Atoms* (Springer, Berlin, 1957), p. 248.